

# Learning-based Fast Electromagnetic Scattering Solver through Generative Adversarial Network

Zhenchao Ma, Kuiwen Xu, *Member, IEEE*, Rencheng Song, *Member, IEEE*, Chao-Fu Wang, *Senior Member, IEEE*, and Xudong Chen *Fellow, IEEE*

**Abstract**—This paper proposes a learning-based non-iterative method to solve electromagnetic (EM) scattering problems utilizing pix2pix, a popular generative adversarial network (GAN). Instead of calculating induced currents directly from a matrix inversion, a forward induced current learning method (FICLM) is introduced to calculate the induced current through a neural-network mapping. The scattered fields can be further calculated through a multiplication of the Green's function with the predicted induced currents. Inspired by wave physics of scattering problems, we have designed three kinds of input schemes, covering different combinations of the given incident field and permittivity contrast, to evaluate the performance of the FICLM model under both single-incidence and multi-incidence cases. Numerical results prove that the proposed FICLM outperforms the method of moments (MoM) in terms of both computational speed and accuracy by use of reference data with a higher precision. The FICLM with the direct sum of permittivity contrast and a so-called Born-type induced current, achieves the best calculation accuracy and generalization capability compared to the other two inputs. The comparison with other types of neural networks, such as U-net, also demonstrates the superior performance of FICLM for dealing with complex scatterers due to the use of adversarial framework in pix2pix. The proposed method paves a new way for the fast solution of EM scattering problems through deep learning techniques.

**Index Terms**—Electromagnetic (EM) scattering, forward induced current learning method (FICLM), Generative adversarial network (GAN), induced currents, method of moments (MoM).

## I. INTRODUCTION

**F**ast and accurate solution of electromagnetic problems plays a crucial role in wireless communication, geophysics, biomedical imaging, and so on [1]–[5]. However, the solution of most electromagnetic problems, governed by Maxwell's equations, cannot be achieved analytically and should rely on various numerical methods. Therefore, the research area of computational electromagnetics (CEM) develops rapidly in recent years. Categorized by the forms of

Maxwell's equations, the CEM methods can be generally divided into two classes: the integral equation based and the partial differential equation (PDE) based ones [6]–[9]. The PDE-based CEM methods include finite difference method (FDM) [10], [11] and finite element method (FEM) [12] etc. The integral-equation-based CEM methods mainly consist of boundary element method [13] (BEM) and method of moments (MoM) and their variants [14], [15] etc.

Since CEM methods solve the Maxwell's equations numerically, the computational complexity is one of the most concerned points for a given method. For example, the implementation of conventional iterative solver for MoM requires  $O(N^2)$  computational and memory complexities, where  $N$  is the number of unknowns. To reduce computational complexity, various fast iterative approaches based on the MoM have been proposed, which are widely used in the electrically large EM scattering problems, e.g., adaptive integral method (AIM) [16], the precorrected fast Fourier transform (pFFT) [17], multi-level fast multipole algorithm (MLFMA) [15], [18], and the multilevel Greens function interpolation method (MLGFIM) [19], [20]. Computational complexities of these approaches are reduced to  $O(N\log N)$ . Although great progresses have been achieved, obtaining full-wave solution with those fast methods is still a time-intensive and resource-consuming task. Therefore, efficient computational electromagnetic solvers that can solve problems in realtime are still urgently needed.

In addition to traditional fast algorithms, some machine learning-based CEM algorithms, such as artificial neural networks (ANN) [21], [22] and least square support vector machine (LS-SVM) [23], have also been proposed to accelerate the CEM calculations. The learning-based CEM approaches essentially approximate some complex mapping through various machine learning techniques. The mapping is then learned from a set of training data to fit the model. Since the time-consuming part is replaced by a fast learning model, the computational complexity of corresponding CEM method is therefore reduced. A good summary of traditional machine learning based CEM methods can be found in [24]. However, owing to the limited model fitting capability and poor hardware resource, the learning-based CEM methods have not received much attention in early stage.

Recently, inspired by the great success of deep learning techniques in computer vision and image processing areas [25], [26], the deep neural networks (DNNs) have been applied to solve some electromagnetic problems [27], such as radar and remote sensing [28], [29], and electromagnetic imaging problems [30]–[33]. As expected, some researchers also have

Manuscript received... The work described was supported by the NSFC under grants No. 61971174, in part by the Talent Project of Zhejiang Association for Science and Technology under Grant SKX201901, and in part by the China Postdoctoral Science Foundation under Grant 2019M661984. (Corresponding author: Kuiwen Xu and Rencheng Song.)

Z. Ma and K. Xu are with Engineering Research Center of Smart Microsensors and Microsystems, Ministry of Education, Hangzhou Dianzi University, Hangzhou 310018, China (e-mail: kuiwenxu@hdu.edu.cn).

R. Song is with the Department of Biomedical Engineering, Hefei University of Technology, Hefei 230009, China (email: rcsong@hfut.edu.cn).

C.-F. Wang is with the Temasek Laboratories, National University of Singapore, Singapore 117411 (e-mail: cfwang@nus.edu.sg).

X. Chen is with the Department of Electrical and Computer Engineering, National University of Singapore, Singapore 117583 (e-mail: elechenx@nus.edu.sg).

tried to devote themselves on solving the Maxwell's equations (or EM scattering problems) with the DNN considering its strong approximation ability for nonlinear mappings. For example, Tang et al. applied the deep learning technique to build a three-dimensional (3-D) electrostatic solver in [34] and Khan et al. [35] investigated the application of deep learning technique to predict the low-frequency magnetic field solution of Maxwell's equations. The results obtained by them have demonstrated that the solvers based on deep learning methods have achieved remarkable performance in terms of both the prediction accuracy and computational time.

In this paper, we try to introduce a new deep learning based method to solve EM scattering problems for a dielectric scatterer located in a predefined spatial domain. The basic idea of our proposed method is to accelerate the calculation of induced currents in MoM. Apparently, the majority calculation of MoM comes from solving the induced current in the state equation built on the whole computational domain [8]. Instead of a direct solution of matrix equation, the proposed forward induced current learning method (FICLM) tries to learn the mapping between the unknown induced current and the given inputs. Physically speaking, the dot product of permittivity contrast  $\bar{\chi}$  with an incident field  $\bar{E}^{inc}$  in the computational domain, i.e.,  $\bar{\chi} \cdot \bar{E}^{inc}$ , can be considered as the Born-type induced current. They have the same size and non-zero support as the solution domain of desired true induced current  $\bar{J}$ . The inputs and the output induced current are all can be considered as the pixel-based images, which share the same pixels in the solution domain. The maps of permittivity contrast, the Born-type induced current, and the true induced current can all be converted to their respective pixel-based images. Therefore, the construction of induced current resulted from given inputs can be considered as an image translation problem in image domain. The pix2pix model [36], a variant from Generative Adversarial Networks (GAN) [37], is a popular framework to solve the image translation problem in computer vision community. Therefore, it is introduced here to approximate the mapping of induced current  $\bar{J}$ . Then, the electromagnetic fields can be calculated through a convolution of the Green's function with the obtained induced current from the pix2pix model.

According to the physical insights of electric field integral equation (EFIE), as discussed in detail in Section II, three different input schemes ( $\bar{\chi}$ ,  $\bar{\chi} \cdot \bar{E}^{inc}$  and their combination or direct sum) are proposed to evaluate the performance of the learning-based method under both single-incidence and multi-incidence cases. In summary, the main contributions of this paper are summarized as follows:

1. FICLM, a data-driven non-iterative learning based electromagnetic scattering method, is proposed to solve the EM scattering problems for a dielectric scatterer located in a predefined spatial domain. Numerical tests have shown that the proposed FICLM outperforms the traditional MoM in terms of both the computational efficiency and calculation accuracy by use of reference data with a higher precision.

2. Three different input schemes are introduced and compared for the FICLM method under both single-incidence and multi-incidence cases. We prove physically and numerically

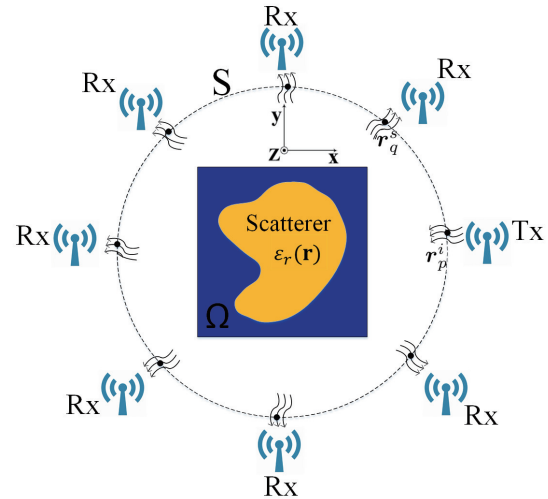


Fig. 1. Geometry of EM scattering problems with the two-dimensional (2-D) transverse magnetic (TM) case. Here Tx and Rx represent the transmitting and receiving antennas, respectively, which are all distributed on the measurement domain  $S$ .

that the FICLM with a combined input  $\bar{\chi} \oplus \bar{\chi} \cdot \bar{E}^{inc}$ , has the best robustness and generalization capability compared to the other two inputs.

3. The proposed FICLM method uses a pix2pix GAN model to approximate the mapping of induced current instead of the commonly-used convolutional neural network. This further enhances the capability of FICLM to predict induced currents for complicated profiles.

The paper is organized as follows. In Section II, the forward induced current learning method (FICLM) for the solution of EM scattering problems is introduced. In Section III, Several benchmark numerical tests are given to verify the interests of proposed methods. A conclusion follows in Section IV.

## II. FORWARD INDUCED CURRENT LEARNING METHOD (FICLM)

### A. Formulation of the forward EM scattering problems

In this section, the forward electromagnetic scattering problem model with the 2-D transverse magnetic (TM) case is introduced and time harmonic fields are deduced with  $\exp(-i\omega t)$  assumption. Note that although the forward problem introduced here is under a 2-D configuration, it can be easily extended to 3-D cases. The configuration of the EM scattering problems is depicted in the Fig. 1. (Actually, the geometry for the EM scattering problems are set for inverse scattering problems [6]).

The computational domain  $\Omega$  is composed by a free space background with permittivity  $\epsilon_0$ , permeability  $\mu_0$  and the scatterers with relative permittivity  $\epsilon_r(\mathbf{r})$ . And the wave number of the homogeneous background medium is denoted as  $k_0 = \omega \sqrt{\epsilon_0 \mu_0}$ . There are  $N_i$  transmitting antennas located at  $\mathbf{r}_p^i$  with  $p = 1, 2, \dots, N_i$  on the observation domain  $S$  to illuminate the computational domain  $\Omega$  sequentially. After the incident waves interacted with the scatterers in the computational domain, the scattered fields are measured by the

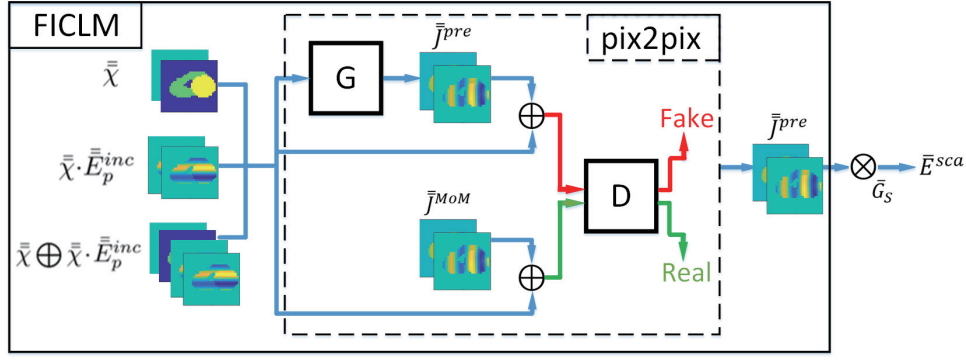


Fig. 2. The overall flow chart of the scheme using the proposed FICLM ( $p$  denotes the index of incidence field, the total number of incidences  $N_i > 1$  denotes the multi-incidence case and  $N_i = 1$  means the single incidence case, which can be considered as a special one of the multi-incidence case).  $\oplus$  denotes the direct sum operator for the input channels and  $\otimes$  denotes the multiplication operator.

receiving antennas located at  $\mathbf{r}_q^s$  with  $q = 1, 2, \dots, N_r$ . Here  $N_r$  denotes the total number of receivers for each incidence.

As opposed to the inverse scattering problems, which are aimed to retrieve the shapes, locations, electric constitutive parameters of the unknown scatterers, the aim of the forward electromagnetic problem is to get the scattered fields with the information of the scatterers in the computational domain and the incidences. Herein, the integral equation based MoM is used for the calculation of the scattered fields.

The interaction of the scattering behavior in the  $\Omega$  can be described with the electric field integral equation (EFIE) [8], [9] and the total electric field in the  $\Omega$  is expressed as

$$E^{tot}(\mathbf{r}) = E^{inc}(\mathbf{r}) + k_0^2 \int_{\Omega} G(\mathbf{r}, \mathbf{r}') \chi(\mathbf{r}') E^{tot}(\mathbf{r}') d\mathbf{r}', \mathbf{r} \in \Omega \quad (1)$$

where  $E^{tot}(\mathbf{r})$  and  $E^{inc}(\mathbf{r})$  are the total and incident electric fields, respectively and  $\mathbf{r}$  and  $\mathbf{r}'$  denote the positions of field point and source point, respectively.  $G(\mathbf{r}, \mathbf{r}') = \frac{i}{4} H_0^{(1)}(k_0 |\mathbf{r} - \mathbf{r}'|)$  represents the 2-D Green's function in free space, where  $H_0^{(1)}(k_0 |\mathbf{r} - \mathbf{r}'|)$  is the first-kind zeroth-order Hankel function and  $\chi(\mathbf{r}') = \epsilon_r(\mathbf{r}') - 1$  is the contrast function. The induced current  $J(\mathbf{r}')$  can be defined as  $J(\mathbf{r}') = \chi(\mathbf{r}') \cdot E^{tot}(\mathbf{r}')$ .

In the observation domain  $S$ , the scattered field  $E^{sca}(\mathbf{r}_q^s)$  measured by a receiver at position  $\mathbf{r}_q^s$ , is also governed by the EFIE with the induced current  $J(\mathbf{r}')$  as

$$E^{sca}(\mathbf{r}_q^s) = k_0^2 \int_{\Omega} G(\mathbf{r}_q^s, \mathbf{r}') J(\mathbf{r}') d\mathbf{r}', \mathbf{r}_q^s \in S. \quad (2)$$

According to [8], the MoM is used to discretize (1) and (2). For convenience, the  $\Omega$  is supposed to be rectangular in order to implement the conjugate gradient fast Fourier transform (CG-FFT) scheme for a fast calculation of scattered fields [38], [39]. The  $\Omega$  is discretized into  $M$  small rectangular cells centered at  $\mathbf{r}_{n_1, n_2}$  with  $M_1, M_2$  being the number of cells along the x and y direction ( $1 \leq n_1 \leq M_1, 1 \leq n_2 \leq M_2$ , and  $M = M_1 \times M_2$ ), respectively. If the discrete cell is small enough, e.g., less than one tenth wavelength, the induced current and the total electric field can be assumed to be constant. Therefore, the corresponding EFIE for (1) can be

discretized as,

$$E_{n_1, n_2}^{tot} = E_{n_1, n_2}^{inc} + \sum_{n'_1, n'_2=1}^{M_1, M_2} G_{D; n_1, n_2; n'_1, n'_2} J_{n'_1, n'_2} \quad (3)$$

where subscript  $n_1, n_2$  denote the indexes of the cell and  $E_{n_1, n_2}^{tot}$ , and  $E_{n_1, n_2}^{inc}$  denote the total and incident electric fields at  $\mathbf{r}_{n_1, n_2}$ , respectively, and  $J_{n'_1, n'_2}$  denotes the induced current source.  $G_D$  indicates the integral of Green's function operator mapping the induced current to the scattered fields in the  $\Omega$  and the analytical expression of  $G_{D; n_1, n_2; n'_1, n'_2}$  over the cells can be found in [6], [8].

Taking into account of all cells in the  $\Omega$ , (3) can be written in a matrix form

$$\bar{E}^{tot} = \bar{E}^{inc} + \bar{G}_D \cdot \bar{J} \quad (4)$$

where  $\bar{E}^{tot} = [E_1^{tot}, E_2^{tot}, \dots, E_M^{tot}]^T$ ,  $\bar{E}^{inc} = [E_1^{inc}, E_2^{inc}, \dots, E_M^{inc}]^T$ ,  $\bar{J} = [J_1, J_2, \dots, J_M]^T$ , the size of the  $\bar{G}_D$  is  $M \times M$ .

The discretized induced current distribution on all cells can be defined as

$$\bar{J} = \bar{\chi}_{diag} \cdot \bar{E}^{tot}. \quad (5)$$

where  $\bar{\chi}_{diag}$  is a diagonal matrix with each element on the diagonal corresponding to the contrast function of the cell located at  $\mathbf{r}_{n_1, n_2}$ . Substituting (4) into (5), we can get

$$\bar{J} = \bar{\chi}_{diag} \cdot (\bar{E}^{inc} + \bar{G}_D \cdot \bar{J}). \quad (6)$$

This is the so-called the state equation.

Similarly, the scattered fields in the observed domain  $S$  governed by (2) can be discretized as,

$$\bar{E}^{sca} = \bar{G}_S \cdot \bar{J}, \quad (7)$$

where  $\bar{E}^{sca} = [E^{sca}(\mathbf{r}_1^s), E^{sca}(\mathbf{r}_2^s), \dots, E^{sca}(\mathbf{r}_{N_r}^s)]^T$ ,  $\bar{G}_S$  is the Green's function operator with the dimensions of  $N_r \times M$  (the coefficient, i.e.,  $k_0^2$ , is included in the formula of  $\bar{G}_S$ ), describing the relationship between the induced current source in the  $\Omega$  to the scattered fields in the measurement domain  $S$ . Eq. (7) is the so-called the data equation.

The conventional MoM firstly solves the induced current  $\bar{J}$  using the following equation

$$\bar{J} = (\bar{I} - \bar{\chi}_{diag} \cdot \bar{G}_D)^{-1} \cdot (\bar{\chi}_{diag} \cdot \bar{E}^{inc}). \quad (8)$$

where  $\bar{I}$  is the identity matrix. The scattered field  $\bar{E}^{sca}$  is then calculated through (7) once the  $\bar{J}$  is obtained from (8).

It is clearly observed from (8) that intensive computational burden of MoM lies in the calculation of  $\bar{J}$ . However, the computation of the inverse matrix  $\bar{Q} = (\bar{I} - \bar{\chi}_{diag} \cdot \bar{G}_D)^{-1}$  is especially burdensome when the  $\Omega$  is electrically large. Herein, in order to implement the solution efficiently, the CG-FFT scheme in [39] is used to get the induced current.

### B. Forward induced current learning method

Herein, in order to connect with the proposed method by image translation solution, all the solution vectors above are reshaped into the pixel-form matrixes. And these pixel-form matrixes, i.e.,  $\bar{\chi}$ ,  $\bar{E}_p^{inc}$ , and  $\bar{J}_p$  ( $p = 1, 2, \dots, N_i$ ), have the same size of  $M_1 \times M_2$  and the same pixels in the solution domain. Here  $p$  denotes the index of incidence field, and in a special case  $N_i = 1$  means the single incidence case.

It is observed from (8) that the induced current is uniquely determined by  $\bar{\chi}$  and  $\bar{\chi} \cdot \bar{E}_p^{inc}$ . And  $\bar{J}_p$ , the 2-D induced current distribution, has the solution domain that is same as the non-zero-value support of  $\bar{\chi}$  and  $\bar{\chi} \cdot \bar{E}_p^{inc}$ . In other words, instead of directly calculating the induced current  $\bar{J}_p$  from (8) by traditional CEM methods, we can use the deep learning-based method with the concept of image translation to obtain the unknown induced current  $\bar{J}_p$  through mapping the known inputs  $\bar{\chi}$  and  $\bar{\chi} \cdot \bar{E}_p^{inc}$ . The inputs, i.e.,  $\bar{\chi}$  and  $\bar{\chi} \cdot \bar{E}_p^{inc}$  and output  $\bar{J}_p$  are all pixel-based “images” and they share the same pixels in the solution domain. This proposed solution method is a typical image-to-image translation process, which can be realized by a GAN framework as illustrated in Fig. 2. Then the output induced current is used to calculate the scattered field.

Inspired by this relationship, we take a famous deep learning-based image translation method, the pix2pix model, to obtain the induced current source  $\bar{J}_p$  directly from input images  $\bar{\chi}$  and  $\bar{\chi} \cdot \bar{E}_p^{inc}$ . This is a data-driven method, where DNNs (generator  $G$  and discriminator  $D$ ) are trained to learn the nonlinear mapping between inputs and outputs. Since the training stage is offline and the DNN calculation is GPU-accelerated, the simulation time of the induced current in MoM can be significantly reduced.

The overall flowchart for the solution of scattered fields is depicted in Fig. 2. The entire procedure consists of two steps. The first step aims to get the induced current with pix2pix model and then in the second step the scattered field can be obtained through a multiplication of the Green’s function  $\bar{G}_s$  with the predicted induced currents in (7). The input of the neural network comes from the known information, i.e., the contrast function  $\bar{\chi}$  and the incident field  $\bar{E}_p^{inc}$  in the computational domain. In the pix2pix model, three schemes with different input information, i.e.,  $\bar{\chi}$ ,  $\bar{\chi} \cdot \bar{E}_p^{inc}$  and  $\bar{\chi} \oplus \bar{\chi} \cdot \bar{E}_p^{inc}$  are proposed and compared. The pix2pix model is firstly trained with training sets and then is tested on the testing sets. The training data set is composed by paired inputs and outputs, which can be obtained by the MoM with CG-FFT.

#### 1) The input schemes of FICLM

The purpose of the FICLM is to calculate the induced currents according to (8) from the knowledge of the scattering process with the pre-defined physical operator  $\bar{G}_D$  and the input variables, e.g.,  $\bar{\chi}$  and  $\bar{E}_p^{inc}$ . In order to express the characteristic relationships of (8) completely, the input of neural network should contain as much prior information as possible. Herein, there are three input schemes proposed, i.e.,  $\bar{\chi}$ ,  $\bar{\chi} \cdot \bar{E}_p^{inc}$  and  $\bar{\chi} \oplus \bar{\chi} \cdot \bar{E}_p^{inc}$ . The third input  $\bar{\chi} \oplus \bar{\chi} \cdot \bar{E}_p^{inc}$ , which consists of 4 channels after spitting  $\bar{\chi}$  and  $\bar{\chi} \cdot \bar{E}_p^{inc}$  into their real and imaginary parts, covers all prior information and ensures that one-to-one corresponding relationship can be achieved. We will evaluate the performance and limitation of different inputs through numerical simulations and comparisons.

When the scatterers are weak (low contrast and/or electrically small size),  $\bar{J}_{p,0} = \bar{\chi} \cdot \bar{E}_p^{inc}$  can be considered as an initialization of the induced currents according to Born approximation. Besides the physically approximated induced current, the third scheme, e.g.,  $\bar{\chi} \oplus \bar{\chi} \cdot \bar{E}_p^{inc}$ , have the additional information of  $\bar{\chi}$  in the inverse matrix operator of (8). Since the pix2pix model is a real-value network, the real and imaginary parts of  $\bar{\chi}$ ,  $\bar{\chi} \cdot \bar{E}_p^{inc}$  and  $\bar{\chi} \oplus \bar{\chi} \cdot \bar{E}_p^{inc}$  are actually used as inputs. Therefore, the numbers of channels for the three input schemes are 2, 2 and 4, respectively.

#### 2) The pix2pix model in FICLM

Since firstly introduced in 2014 by Ian Goodfellow, various variants of GAN have been proposed such as the deep convolutional GAN (DCGAN) [40], Wasserstein GAN (WGAN) [41], conditional GAN (CGAN) [42], Cycle-GAN [43], pix2pix-GAN [36] and so on. Pix2pix has good performances in image-to-image translation problems, such as synthesizing photos from label maps, reconstructing objects from edge maps, and coloring images, and so on [36]. Compared with some other networks for image translation task, such as the U-net, pix2pix has been proven to own better prediction capability in processing imaging tasks [36]. According to the processing EM scattering problems, the reason that we choose pix2pix model is twofold. First, the pix2pix model was designed for the image-to-image translation task. The inputs of FICLM are the combinations of incident field  $\bar{E}_p^{inc}$  and permittivity contrast  $\bar{\chi}$ . Since the  $\bar{\chi}$  has the same effective support as the solution domain of induced current, this is a perfect image translation problem. Second, the pix2pix is based on conditional GAN and it takes the input images as the condition. Therefore, the pix2pix model can better guide the generation of output image by adding additional information to the model.

The pix2pix of GAN is composed of two networks, the generator network  $G$  and the discriminator network  $D$ . The generator  $G$  maps an input image to the target image. As presented in Fig. 3,  $G$  has a similar network structure as the U-net, where the mirrored downsampling and upsampling layers are skipingly connected.  $G$  can be understood as an encoder-decoder structure with skip connections between the mirrored layers. Different from the original pix2pix which processes the images with pixel values ranging from 0 to 255 in imaging processing, the actual true values of the induced currents are generated through  $G$  by removing the last nonlinear  $\tanh()$  activation layer in the network.

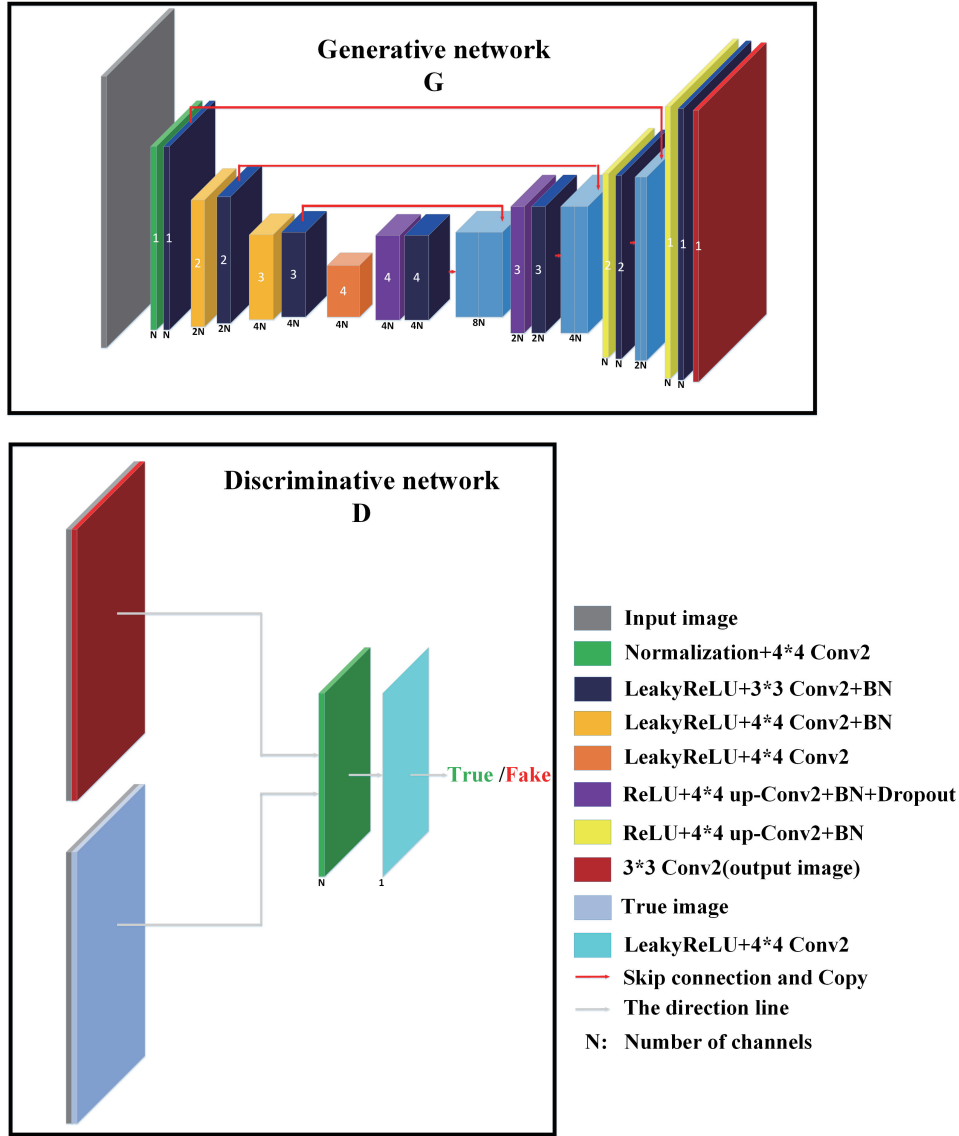


Fig. 3. The configuration of generative network ( $G$ ) and discriminative network ( $D$ ).

The purpose of network of  $D$  is to discriminate the predicted picture from the real ground truth. Since the pix2pix model is a conditional GAN method, the inputs of  $D$  include not only the predicted image but also the input image as the conditional information. In pix2pix, the output of the discriminator  $D$  is designed to be a feature vector instead of the commonly used scalar value. This enables  $D$  to make a finer discrimination on the image in a patch level, i.e., the receptive field for one component of the feature vector corresponding to a image patch. Therefore, the pix2pix model with the specially designed  $D$  is also referred as the PatchGAN. Other detailed explanations for the pix2pix model can be referred to [36].

### 3) Loss functions of the pix2pix model in FICLM

The loss functions of  $G$  and  $D$  in pix2pix can be defined in least squares as

$$\min_D L(D) = \frac{1}{2} E_{x, J_{\text{MoM}}} [D(x, J_{\text{MoM}}) - 1]^2 + \frac{1}{2} E_x [(D(x, G(x)))^2], \quad (9)$$

$$\min_G L(G) = \frac{1}{2} E_x [(D(x, G(x)) - 1)]^2 + \lambda L_{L1}(G), \quad (10)$$

where  $x$  denotes the input variables for pix2pix model, and  $J_{\text{MoM}}$  denotes the ground truth induced current calculated by MoM.  $E$  is the expectation function,  $\lambda$  is a hyperparameter, and  $L_{L1}(G)$  is a  $L_1$ -norm pixel-wise loss defined as

$$L_{L1}(G) = E_{x, J_{\text{MoM}}} [\|J_{\text{MoM}} - G(x)\|_1]. \quad (11)$$

The losses of least square GAN in (10) and (11) are considered to be more stable and easily to converge than that of the vanilla GAN with binary cross-entropy loss [44]. Besides, the use of  $L_{L1}(G)$  in  $G$  loss can enforce the generator not only to fool the discriminator but also to generate output which is close to the ground truth.

The  $G$  and  $D$  are trained alternatively in an adversarial way until a Nash equilibrium (namely a balance between the  $G$  and  $D$ ) is reached. Namely, the data generated by the generator  $G$

is very close to the real sample, and the discriminator  $D$  cannot distinguish it from the real data.

### C. Computational complexity

The computational efficiency plays a key role in the forward scattering problems. So, it is important to analyze the computational complexity of the calculation of the scattered field by the proposed non-iterative method compared with the traditional methods. The computational complexity of the proposed FICLM can be divided into three parts: the preparation of network input is labeled as  $C_1$ , the forward calculation of neural network  $G$  to predict the induced current is labeled as  $C_2$ , and the third part to calculate the scattered field with the predicted current is labeled as  $C_3$ .

As mentioned above, the  $\Omega$  is discretized into  $M$  small rectangular subunits. For the input of FICLM ( $\bar{\chi}$ ,  $\bar{\chi} \cdot \bar{E}_p^{inc}$ ,  $\bar{\chi} \oplus \bar{\chi} \cdot \bar{E}_p^{inc}$  as inputs), the computational costs are dominated by computing the  $\bar{\chi}$  and  $\bar{E}_p^{inc}$  both require  $O(M)$ . The computational cost to compute the multiplication of two matrices or vector, such as the dot multiplication of  $\bar{E}_p^{inc}$  and  $\bar{\chi}$ , is  $O(M)$ . Therefore, the computational cost of this part is  $C_1 = O(M)$  for each input sample.

The next part is the pix2pix GAN to predict the mapping for the induced current. The computational cost is composed of the several basic operations in the neural networks, such as the leakyReLU, ReLU, BN, where the complexity is dominated by the operation of convolutions. Specifically, in the pix2pix,  $Q_i$  and  $Q_o$  are supposed to the numbers of input feature maps and output feature maps, respectively and the size of feature maps are  $M(M = M_1 \times M_2 = 1024)$ . The convolution kernel size is  $K_f \times K_f (K_f = 4$  in this paper). Considering the above training parameters of the networks, the computational workload in the convolution layer is in the order of  $C_2 = O(Q_i Q_o M K_f^2)$ .

We have investigated the performance with different number of layers for the network of  $G$ . Considering to balance the computational time, complexity, and the calculation accuracy, the generator  $G$  consisting of 16 layers is used for the prediction of the unknown induced current. Consequently, there are altogether 16 convolution layers (consisting of 8 number of  $3 \times 3$  convolution layers and 8 number of  $4 \times 4$  convolution layers) in the  $G$  architecture of this paper, and the number of channels in the convolution layers is much bigger than the channels in the input layer, so the computational costs in different schemes as input of FICLM are not far apart.

To calculate the scattered fields, the computational cost of matrix-vector multiplication is  $C_3 = O(N_r M)$ , which can be referred to the formula (7).

The simulation times for the three methods to calculate the forward induced currents, i.e., the direct inverse matrix method, the CG-FFT-based method, and the FICLM, are given in TABLE I. It is worth mentioning that the neural networks are accelerated by GPU-based parallelized calculation. A server with Intel(R) Core(TM) i7-8700K CPU, 32G RAM, and GeForce GTX 2080Ti GPU is used for both training and testing. In the testing stage, it only requires one non-iterative process by utilizing  $G$  network to obtain the induced current.

From the statistically analysis, it takes about 0.25 seconds to get the induced currents with 100 samples and by contrast, more than 10 times cost is spent by the fast MoM with CG-FFT, and more than 25 times cost is spent by the direct inverse matrix method.

TABLE I  
CONSUMPTION TIME TO CALCULATE THE INDUCED CURRENTS FOR 100 SAMPLES.

Method	Direct inverse matrix method	CG-FFT-based MoM	FICLM
Time (seconds)	6.43	2.61	0.25

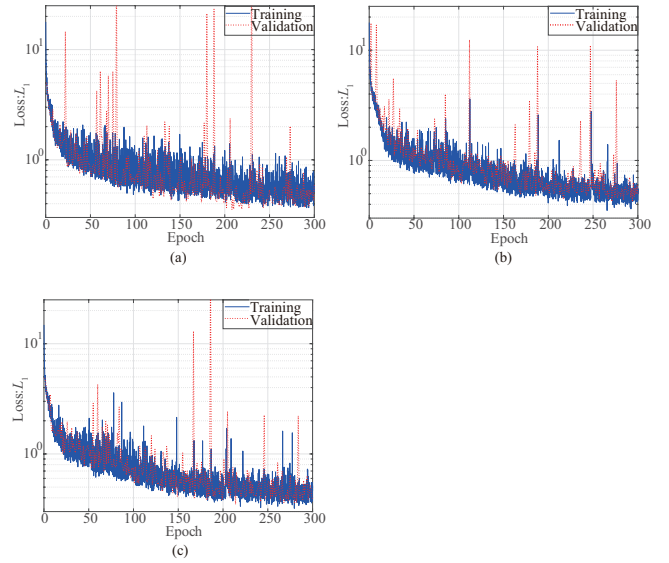


Fig. 4. The  $L_1$  loss for the single-incidence case. (a), (b) and (c) denote the losses of pix2pix with  $\bar{\chi}$ ,  $\bar{\chi} \cdot \bar{E}_p^{inc}$  and  $\bar{\chi} \oplus \bar{\chi} \cdot \bar{E}_p^{inc}$  as inputs, respectively. The blue line and the red line denote the training curve and validation curve, respectively.

### III. NUMERICAL RESULTS

In this section, several numerical tests are presented to evaluate the feasibility of the proposed data-driven FICLM network. In order to compare the performance of three different kinds of input schemes, i.e.,  $\bar{\chi}$ ,  $\bar{\chi} \cdot \bar{E}_p^{inc}$ ,  $\bar{\chi} \oplus \bar{\chi} \cdot \bar{E}_p^{inc}$ , the numerical tests are divided into two categories, the single-incidence case and multi-incidence case.

For the single-incidence case, there is only one transmitting antenna located at a fixed angle, e.g., 180 degree. For the multi-incidence case, there are multiple transmitting antennas located at different angles. The plane wave is used as the incident wave in both cases.

In the training stage, the MoM is used to generate the reference induced current for each given profile and incident wave. To evaluate the quality of the reconstructed induced current for a single profile under a single incidence, the mean absolute error  $L_{single}$  is defined as below

$$L_{single} = \frac{1}{M} \sum_{i=1}^{M_1} \sum_{j=1}^{M_2} abs(\bar{J}_{MoM}^{i,j} - \bar{J}_{pix2pix}^{i,j}) \quad (12)$$

where  $i, j$  denote the index of grids along the x axis and y axis (row and column), respectively.  $\bar{J}_{\text{MoM}}$  and  $\bar{J}_{\text{pix2pix}}$  denote the reference induced current and the calculated one by pix2pix, respectively. Similarly, to evaluate the overall merits of the methods, the average of  $L_{\text{single}}$  errors on all samples within the testing set is defined as,

$$L_{\text{mean}} = \frac{1}{N} \sum_{k=1}^N L_{\text{single},k}, \quad (13)$$

where  $N$  denotes the total number of samples within the testing set, and  $L_{\text{single},k}$  indicates the mean absolute error of the  $k$ th sample.

### A. Numerical Setup

In all of the numerical tests, the  $\Omega$  is a square with the size of  $2 \times 2 \text{ m}^2$  centered at the origin and is discretized into  $32 \times 32$  grids for the calculation of induced currents. In order to get more reliable reference induced currents, we first calculate the induced current of each sample by MoM with  $64 \times 64$  dense grids, which is denoted as  $\bar{J}_{64}$ . The reference induced current map used in the training stage by FICLM, which is termed as  $\bar{J}_{64 \text{ to } 32}$ , is down sampled from the  $\bar{J}_{64}$  to a  $32 \times 32$  size. The input data is paired with the corresponding reference output  $\bar{J}_{64 \text{ to } 32}$ , which composes the training dataset for the pix2pix model in FICLM. The corresponding calculated induced current through FICLM is defined as  $\bar{J}_{\text{pix2pix}}$ . The induced current calculated directly by MoM with  $32 \times 32$  grids, i.e.,  $\bar{J}_{32}$ , is used to compare the accuracy by the proposed learning-based method with the conventional MoM. In all tests, the operating frequency is set at 400 MHz, corresponding to a wavelength  $\lambda = 0.75 \text{ m}$  in the air background medium. There are 32 receivers uniformly arranged on a circle to collect the scattered fields, where the circle is centered at the origin with a radius equals to 3 m.

The scatterer profiles of training dataset are chosen as handwritten digits between 0 to 9 from the MNIST database that can be downloaded at <http://yann.lecun.com/exdb/mnist/>. In order to supply more diverse samples, a random circle is generated in the domain  $\Omega$  to overlap with the digit, where the overlapping parts belong to the cylinder. The relative permittivities of the profiles in MNIST database and the circles are randomly taken from 1.01 to 1.50. And the radii of the circles are between 0.15m and 0.5m.

For the single-incidence case, the angle of incident field is fixed at  $180^\circ$ . For the multi-incidence case, the angles of incidence are set uniformly between  $0^\circ$  and  $360^\circ$  with a  $10^\circ$  difference.

In general, the number of training samples depends on the complexity of the network we use. The more complex the neural network is, the larger number of training samples should be used to train the model. Consequently, there is a tradeoff between the model accuracy and the training time cost. We have done several tests with different sizes of training samples. In terms of the model prediction accuracy for testing and the computational cost for training, the total number of samples for the single-incidence and multi-incidence cases are set as 10500 and 21000, respectively. For the single-incidence case,

9500 samples are used for training, 500 samples for validation, and another 500 samples for testing. Whereas, for the multi-incidence case, 19000 samples are used for training, 1000 samples for validation, and another 1000 samples for testing.

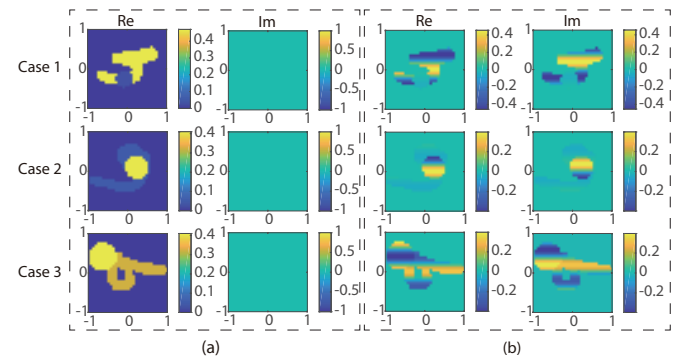


Fig. 5. The three different input schemes of pix2pix with the incidence of plane wave for single-incidence cases (three different cases corresponding to the different rows): (a) the first scheme with two channels of  $\text{Re}(\bar{\chi})$  (left column) and  $\text{Im}(\bar{\chi})$  (right column); (b) the second scheme with two channels of  $\text{Re}(\bar{\chi} \cdot \bar{E}_p^{\text{inc}})$  (left column) and  $\text{Im}(\bar{\chi} \cdot \bar{E}_p^{\text{inc}})$  (right column). The third scheme are with four channels of direct sum of  $\bar{\chi} \oplus \bar{\chi} \cdot \bar{E}_p^{\text{inc}}$ . Herein “Re” and “Im” denote the real and imaginary parts, respectively.

In order to statistically analyze the performance of the proposed methods, two different sets are used for testing. One is the MNIST database with a randomly distributed cylinder in the  $\Omega$ , which is similar with the training set. The other is composed of two randomly located cylinders in the  $\Omega$ , termed as ‘Cylinders’. And the value of relative permittivities for the two cylinders are taken from 1.01 to 1.50 randomly with the radii varying from 0.15m to 0.5m independently.

### B. Implementation Details

In the pix2pix network, there are several hyperparameters to be chosen carefully. Those parameters are usually problem dependent and need to be set heuristically.

1) *Output dimension of discriminator D*: The output dimension of discriminator  $D$  is one of the most important factors affecting the quality of the predicted result. When the output dimension of discriminator  $D$  is larger than one, it is denoted as the patchGAN [44]. The output of PatchGAN is not a scalar value, but a matrix. And each element in the matrix signifies whether the corresponding small patch in the image is “real” or “fake”. If the size of patchGAN is too small, it may cause the discriminator  $D$  difficult to identify the local area of the image. Conversely, there are too many parameters to be optimized if the size of patchGAN is too large. Different size of patchGAN can be achieved by designing the convolutional layers of  $D$  network. And we have tested the different sizes of the patchGAN to compare the performance with each other. Through the numerical comparison, the output dimension of discriminator  $D$  is selected as  $15 \times 15$ .

2) *Learning rate*: Learning rate, as an important parameter in deep learning network, determines the scaling factor (step size) in the update direction. If the learning rate is too small, the convergence would become very slow. Whereas the learning rate is large, the gradient may oscillate around

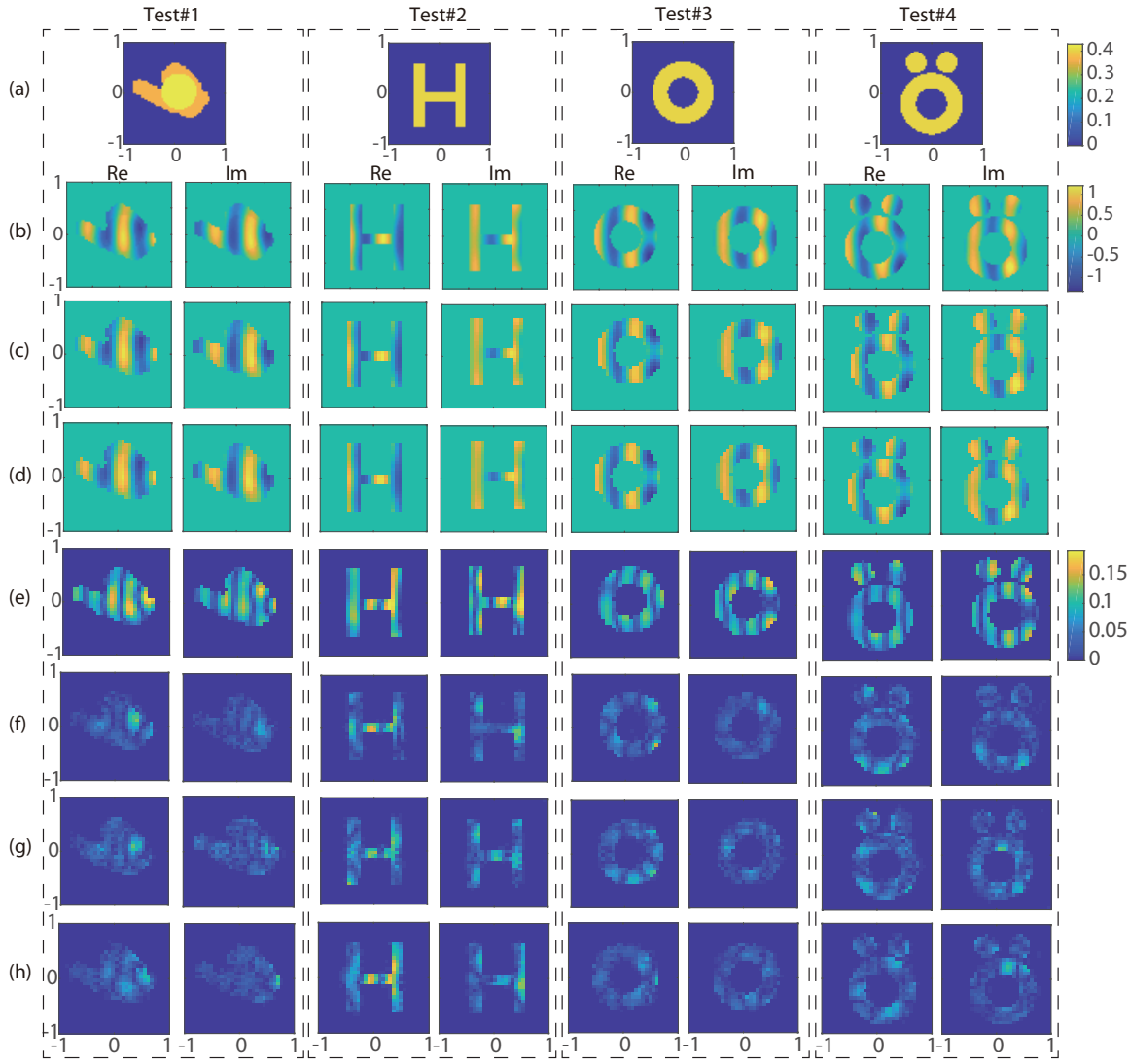


Fig. 6. Test with single-incidence case illustrated by plane wave. (a) the exact profiles for four Test# 1-4, (b) the induced current calculated by MoM with  $64 \times 64$  grids ( $\bar{J}_{64}$ ), (c)  $\bar{J}_{64to32}$  sampling the induced current  $\bar{J}_{64}$  at equal intervals, (d) the induced current calculated by MoM with  $32 \times 32$  grids (denoted as  $\bar{J}_{32}$ ), (e) the difference value between the reference one, i.e.,  $\bar{J}_{64to32}$ , and  $\bar{J}_{32}$ , (f-h) the difference values between the reference one, i.e.,  $\bar{J}_{64to32}$ , and the three different schemes, i.e.,  $\bar{\chi} \cdot \bar{E}_p^{inc}$ ,  $\bar{\chi} \oplus \bar{\chi} \cdot \bar{E}_p^{inc}$ , respectively. For convenience, the induced current shown here has been multiplied by 100 times.

the local minimum value and the network fails to converge. Through continuous testing, the learning rates of  $G$  network and  $D$  network are both set to 0.0002 initially, and they are reduced by half per 100 epochs.

3) *Batch size*: Batch size refers to the number of samples used in one iteration, which affects the optimization level and training speed of the model. It will lead to extremely slow rate of convergence with small batch size. On the contrary, if the batch size is too big, the generalization ability of network will become worse. By numerical comparison, the batch size is set as 64.

4) *The regularization parameter  $\lambda$* : The hyperparameter  $\lambda$  is used to regularize the relative effects of the two loss functions (GAN-loss and  $L_1$  loss) in the objective function. In this study, we find that it has good performance by setting the hyperparameter  $\lambda$  as 100.

For the single-incidence case, it takes about 40 minutes for the training of the neural network. Fig. 4 illustrates the results

of the  $L_1$  loss in the training for a single-incidence case. It can be seen clearly that the proposed FICLM algorithm has converged well with all three different schemes. In the following, the numerical results for both single-incidence and multi-incidence cases are discussed in detail.

### C. Test with the single-incidence case

In the single-incidence case, the transmitter is located at  $180^\circ$ . In the training, the relative permittivities of the scatterers are set from 1.01 to 1.50 randomly. Fig. 5 illustrates an example of input images for FICLM under three different schemes.

As is shown in Fig. 5, for the first and second schemes, the number of input channels is set as 2, consisting of both real part and imaginary part. The third scheme  $\bar{\chi} \oplus \bar{\chi} \cdot \bar{E}_p^{inc}$ , which combines the first and second schemes, occupies 4 channels as the input of FICLM.

TABLE II  
THE MEAN ABSOLUTE ERRORS FOR THE DIFFERENT TESTS IN FIG. 6 WITH RESPECT TO  $\bar{J}_{64to32}$ .

example	Test #1	Test #2	Test #3	Test #4	MNIST	Cylinders
$\epsilon_r$	1.36 1.43	1.40	1.40	1.40	/	/
$J_{32}$	2.80%	2.29%	2.29%	2.90%	1.87%	1.23%
$J_{pix2pix}$ ( $\bar{\chi}$ )	0.91%	1.19%	0.97%	1.47%	0.95%	0.48%
$J_{pix2pix}$ ( $\bar{\chi} \cdot \bar{E}_p^{inc}$ )	0.99%	1.29%	1.05%	1.42%	0.84%	0.59%
$J_{pix2pix}$ ( $\bar{\chi} \oplus \bar{\chi} \cdot \bar{E}_p^{inc}$ )	0.94%	1.49%	0.85%	1.30%	0.72%	0.42%

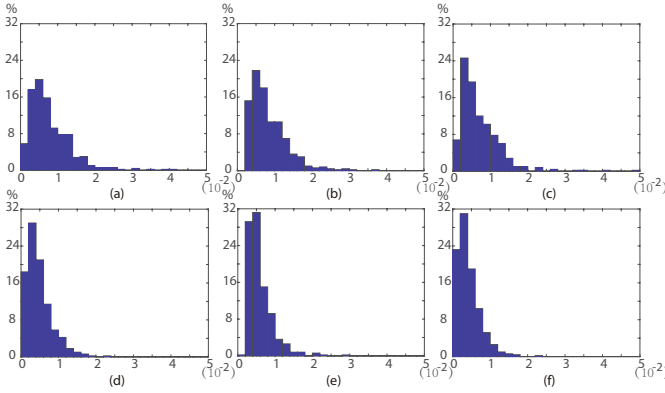


Fig. 7. The loss histograms over testing results for the single-incidence case. (a)-(c) denote the histograms of MNIST test set with  $\bar{\chi}$ ,  $\bar{\chi} \cdot \bar{E}_p^{inc}$  and  $\bar{\chi} \oplus \bar{\chi} \cdot \bar{E}_p^{inc}$  as the inputs of the network, respectively. (d)-(f) denote the histograms of “Cylinders” test set with  $\bar{\chi}$ ,  $\bar{\chi} \cdot \bar{E}_p^{inc}$  and  $\bar{\chi} \oplus \bar{\chi} \cdot \bar{E}_p^{inc}$  as the inputs of the network, respectively.

There are four different tests altogether. The Test#1 selects a profile randomly from the training database. The Test#2 has a profile of Latin letter “H”. And the other two tests, denoted as “ring” and “Austria”, are totally different from the profiles in the MNIST training database. The relative permittivities of these scatterers for the four tests are shown in TABLE II. The predicted results by FICLM for the four tests are presented in Fig. 6. The Fig. 6(b) shows the induced currents with  $64 \times 64$  dense grids. After a uniform down-sampling, the reference induced current for FICLM is depicted in Fig. 6(c). The induced current  $\bar{J}_{32}$  calculated directly by MoM with coarse  $32 \times 32$  grids is illustrated in Fig. 6(d). The difference image between  $\bar{J}_{32}$  and the reference  $\bar{J}_{64to32}$  is shown in Fig. 6(e). Similarly, the differences between the predicted induced current  $\bar{J}_{pix2pix}$  and the reference  $\bar{J}_{64to32}$ , are illustrated in Fig. 6(f)-(h) for three different input schemes, respectively. As seen from Fig. 6(e)-(h), the errors calculated by FICLM with three different schemes are all lower than the  $\bar{J}_{32}$  calculated directly by MoM in Fig. 6(e).

The absolute mean error  $L_{single}$  for the four test examples and two test sets (consisting of the MNIST and Cylinders) are listed in TABLE II. Fig. 7 illustrates the histograms of tested results over two test sets with three different input schemes. The results above all prove that the accuracy of FICLM is much better than the MoM with the same grids. Although the profile in Test#2 is totally different from the training samples, the performance of the proposed FICLM is also satisfied and even better than the one by MoM. It is validated from both

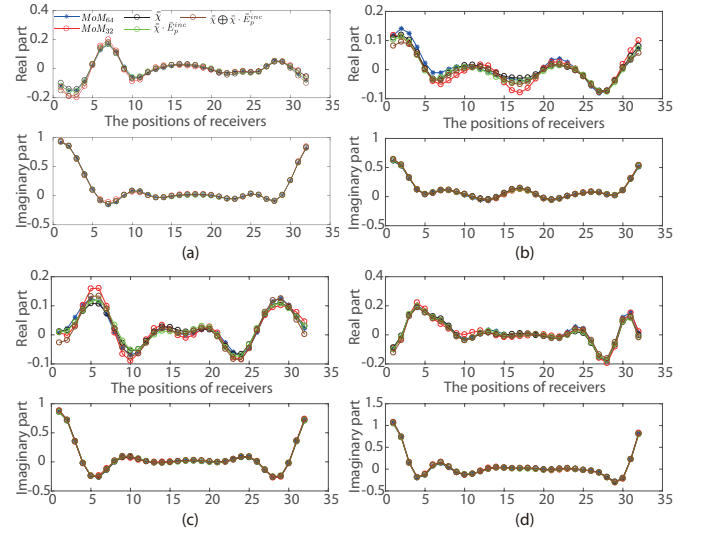


Fig. 8. The calculated scattered fields with the predicted induced currents in Fig. 6 for Test# 1 to 4. (a) Test #1, (b) Test #2, (c) Test #3, (d) Test #4. The blue line “—” with “\*” is taken as a reference calculated by MoM using  $\bar{J}_{64}$ . The red line “—” with “o” denotes the scattered fields calculated by MoM with the induced current, i.e.,  $\bar{J}_{32}$ . The black line “—”, green line “—” and the brown line “—” with “o” denote the results of scattered fields with the first, second and third schemes, respectively.

the Test #1-4 and two test sets that the performance of FICLM with three different input schemes are almost at the same level. This is because the incidence field is fixed and kept to be the same in both the training and testing stages. In other words, the FICLM network also learns the information of incidence for the first two input schemes.

After obtaining the induced current by FICLM, the scattered fields can be gotten by (7), where the results for Test# 1-4 are depicted in Fig. 8(a)-(d). It shows that the real parts and imaginary parts of the calculated scattered fields are quite consistent to the reference ones calculated by MoM with dense  $64 \times 64$  grids. Consequently, for the single-incidence case, the proposed learning-based forward solver FICLM can well predict the induce currents in the  $\Omega$  with all the input of three schemes, and the method also exhibits good generalization capability for scatterers with totally different shapes.

#### D. Test for the single-incidence case with varying incident intensities

In the above tests, the incident intensity and angle is fixed such that the incidence field can be considered as a constant. In order to further compare the generalization capability and robustness for the different input schemes, in this section, we give another single-incidence test with varying incident intensities. All of the basic configurations and settings in the training stage are almost the same as those in Section C. However, in the training stage, here we simulate varying incident fields instead of a fixed one by multiplying a coefficient  $\alpha$  to the plane incident wave. The transmitting angle is still at 180 degrees. The coefficient  $\alpha$  is chosen randomly from an interval  $[0.4, 1]$ .

In order to benchmark with results of Section C, in the test processing, the  $\bar{\chi} \cdot \bar{E}_p^{inc}$  with the same value is selected as

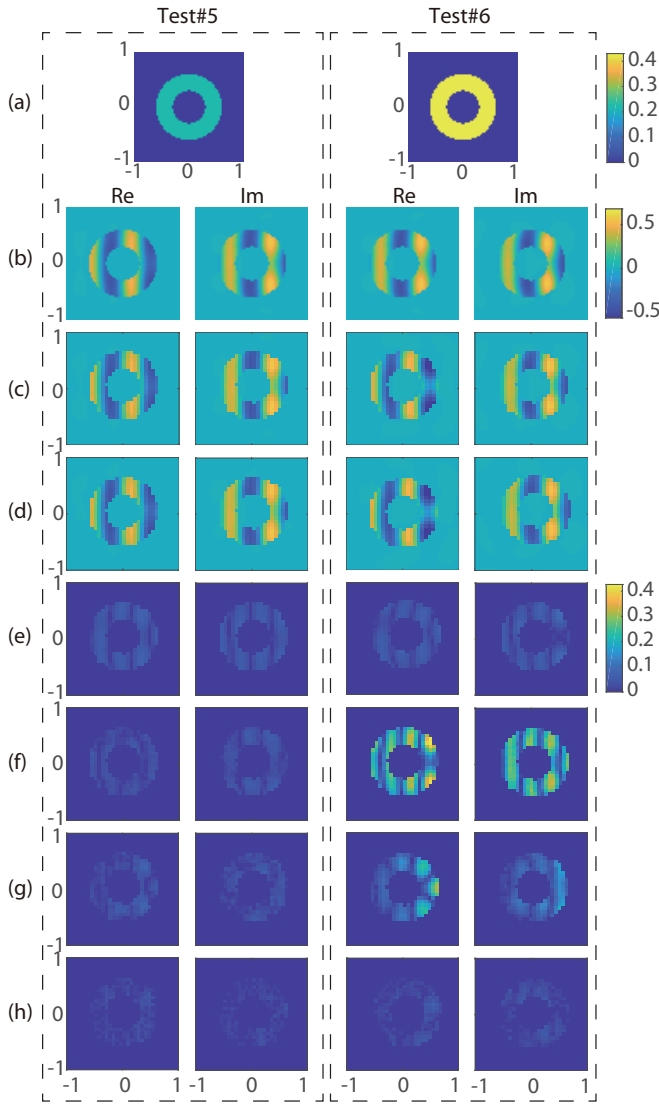


Fig. 9. Tests of the single-incidence case under the different incident intensity. (a) the exact profiles for Test# 5-6, (b) the induced current calculated by MoM with  $64 \times 64$  grids ( $\bar{J}_{64}$ ), (c)  $\bar{J}_{64to32}$  sampling the induced current  $\bar{J}_{64}$  at equal intervals, (d) the induced current calculated by MoM with  $32 \times 32$  grids (denoted as  $\bar{J}_{32}$ ), (e) the difference value between the reference one, i.e.,  $\bar{J}_{64to32}$ , and  $\bar{J}_{32}$ , (f)-(h) the difference values between the reference one, i.e.,  $\bar{J}_{64to32}$ , and the three different schemes, i.e.,  $\bar{\chi}$ ,  $\bar{\chi} \cdot \bar{E}_p^{inc}$ ,  $\bar{\chi} \oplus \bar{\chi} \cdot \bar{E}_p^{inc}$ , respectively. For convenience, the induced current shown here has been multiplied by 100 times.

the test examples. Therefore, the contrast  $\chi$  becomes  $\bar{\chi}/\alpha$ , while the corresponding incident field is  $\bar{E}_p^{inc} \cdot \alpha$ . In such a configuration, the incident field  $\bar{E}_p^{inc} \cdot \alpha$  and the contrast  $\bar{\chi}/\alpha$  will lead to physically different induced current when  $\alpha$  varies. But their product is still kept the same as  $\bar{\chi} \cdot \bar{E}_p^{inc}$ . For the FICLM with the second scheme  $\bar{\chi} \cdot \bar{E}_p^{inc}$  as the input, the predicted induced current will not change along with  $\alpha$ . Similarly, for the first scheme, there is no information of incident fields in the input of network.

To validate the above analysis, two special tests (Test#5 and 6) are given, as shown in Fig. 9. The profiles in both the two tests are a single ring and the contrast values for Test# 5 and Test# 6 are 0.2 and 0.4, respectively. The corresponding

TABLE III  
THE MEAN ABSOLUTE ERRORS FOR THE DIFFERENT EXAMPLES IN FIG. 9 WITH RESPECT TO  $\bar{J}_{64to32}$ .

example	Test#5	Test#6	MNIST	Cylinders
$\epsilon_r$	1.20	1.40	/	/
$J_{32}$	1.19%	1.15%	1.86%	1.23%
$J_{pix2pix}(\bar{\chi})$	0.78%	5.93%	3.24%	2.17%
$J_{pix2pix}(\bar{\chi} \cdot \bar{E}_p^{inc})$	0.74%	2.50%	3.69%	2.07%
$J_{pix2pix}(\bar{\chi} \oplus \bar{\chi} \cdot \bar{E}_p^{inc})$	0.41%	0.54%	1.15%	0.55%

intensity of the incident wave is 1 and 0.5, respectively. The calculated results for the two tests are depicted in Fig. 9. The errors distribution profiles for three scheme are shown in Fig. 9(f)-(h) and the quantitative errors for the Test#5 and 6 and the two test sets are summarized in TABLE III. It can be seen clearly that the performance of the third scheme is much better than the other two schemes. From the average errors of two test databases, it is verified that the third scheme of the proposed method has better versatility and stability compared to other two schemes. Also, after comparing the results in Fig. 9(e) to Fig. 9(h) and the quantitative errors in Table III, it shows that the performance of the proposed FICLM method with the third scheme is better than the one gotten by MoM in terms of both accuracy and efficiency.

### E. Test with multi-incidence cases

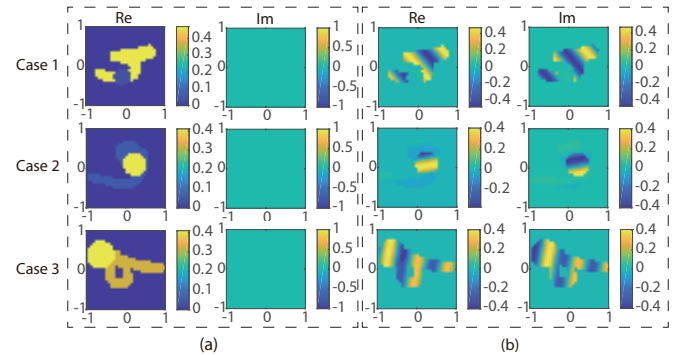


Fig. 10. The inputs of pix2pix with multi-incidence. (a)  $\bar{\chi}$ ; (b) the second scheme,  $\bar{\chi} \cdot \bar{E}_p^{inc}$ ; and (a)  $\oplus$  (b) is the third scheme,  $\bar{\chi} \oplus \bar{\chi} \cdot \bar{E}_p^{inc}$ . The incidence angels for the 1st, 2nd and 3rd examples (rows) are  $310^\circ$ ,  $10^\circ$ , and  $80^\circ$ , respectively.

TABLE IV  
THE MEAN ABSOLUTE ERROR FOR THE EXAMPLES IN FIG. 11 WITH RESPECT TO  $\bar{J}_{64to32}$ .

example	Test#7	Test#8	Test#9	Test#10	MNIST	Cylinders
$\epsilon_r$	1.36 1.43	1.40	1.40	1.40	/	/
angle	$120^\circ$	$180^\circ$	$175^\circ$	$185^\circ$	/	/
$J_{32}$	3.54%	2.29%	2.50%	2.61%	1.84%	1.18%
$J_{pix2pix}(\bar{\chi} \cdot \bar{E}_p^{inc})$	0.96%	1.50%	1.28%	2.55%	1.27%	0.91%
$J_{pix2pix}(\bar{\chi} \oplus \bar{\chi} \cdot \bar{E}_p^{inc})$	1.10%	1.45%	1.33%	2.83%	1.15%	0.86%
$J_{U-net}(\bar{\chi} \cdot \bar{E}_p^{inc})$	3.59%	6.27%	4.36%	8.07%	4.85%	3.56%
$J_{U-net}(\bar{\chi} \oplus \bar{\chi} \cdot \bar{E}_p^{inc})$	3.92%	5.94%	4.55%	8.62%	5.58%	3.97%

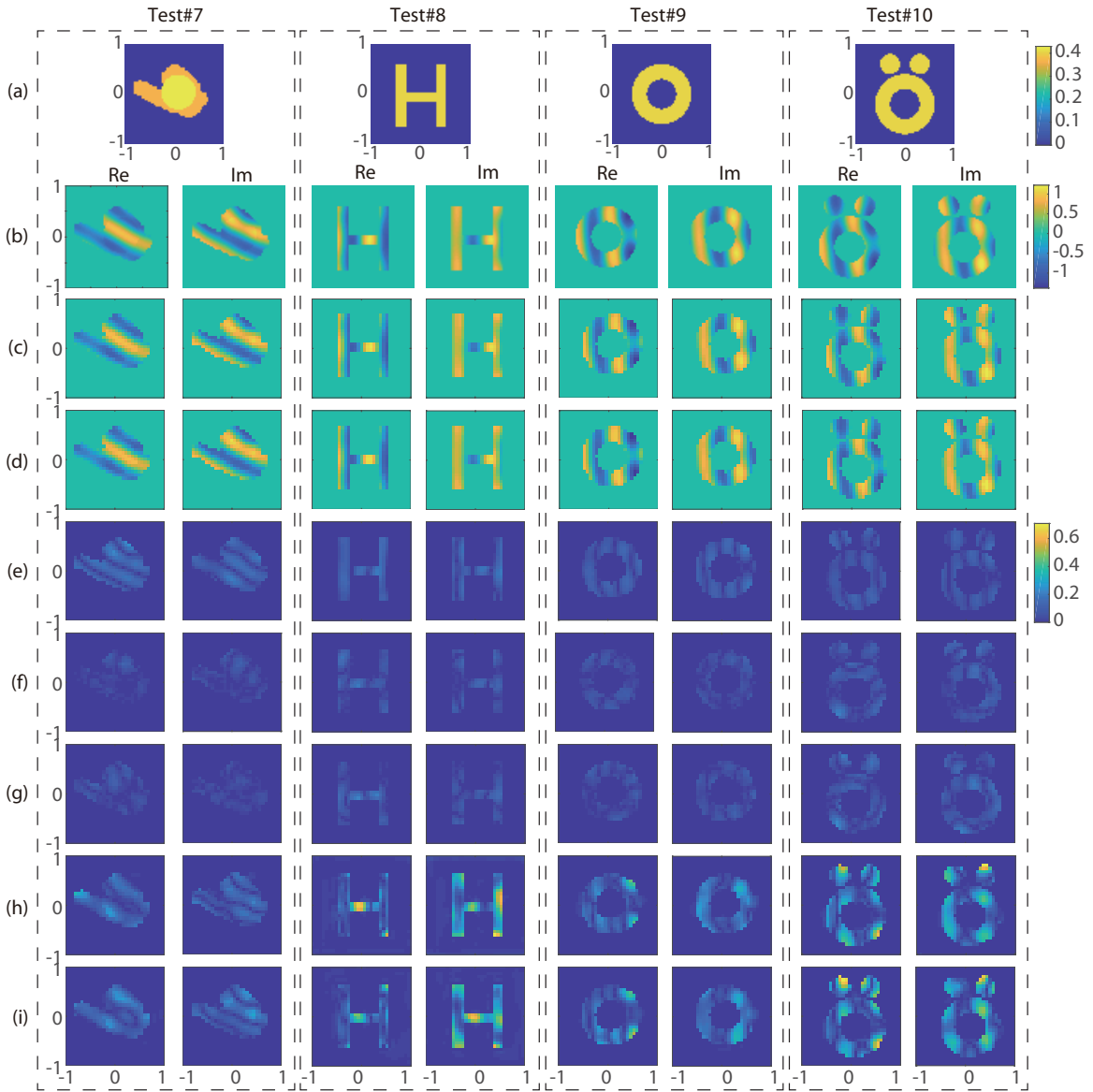


Fig. 11. Tests for the multi-incidence cases illustrated by plane wave using the proposed FICLM. (a) the exact profiles for four Test# 7-10, (b) the induced current calculated by MoM with  $64 \times 64$  grids ( $\bar{J}_{64}$ ), (c)  $\bar{J}_{64to32}$  sampling the induced current  $\bar{J}_{64}$  at equal intervals, (d) the induced current calculated by MoM with  $32 \times 32$  grids (denoted as  $\bar{J}_{32}$ ), (e) the difference value between the reference one, i.e.,  $\bar{J}_{64to32}$ , and  $\bar{J}_{32}$ , (f)-(g) the difference values between the reference one, i.e.,  $\bar{J}_{64to32}$ , and the two different schemes, i.e.,  $\bar{\chi} \cdot \bar{E}_p^{inc}$ ,  $\bar{\chi} \oplus \bar{\chi} \cdot \bar{E}_p^{inc}$ , respectively. (h)-(i) the difference values between the reference one, i.e.,  $\bar{J}_{64to32}$  and the one calculated with second and third schemes by U-net. For convenience, the induced current shown here has been multiplied by 100 times.

To further validate the versatility of the proposed FICLM, the multi-incidence cases are tested in this section. In the multi-incidence case, the angles of incidence are uniformly sampled from  $0^\circ$  to  $360^\circ$  with a  $10^\circ$  step. Since the angles of incident field are varying, the first scheme is not valid any more in such case. Therefore, the second and third schemes are used for the inputs of the neural networks in the multi-incidence case. The profiles of the contract function for three examples in the training are shown in Fig. 10(a). The input profiles for the different incidence angles, i.e,  $310^\circ$ ,  $10^\circ$ , and  $80^\circ$ , are depicted in the first, second, and third rows of Fig. 10(b). The other parameter settings are the same as the single-incidence case.

Also there are four tests for the multi-incidence case. Test#7

has a profile randomly selected from the training database with the relative permittivity of 1.36 and 1.43 for the MNIST profile and embodied ‘‘Cylinders’’ profile under an incident angle of  $120^\circ$ . Test #8, #9 and #10 are the same profiles as the ones in Fig. 6 for the single-incidence case. But the incident angles are  $180^\circ$ ,  $175^\circ$  and  $185^\circ$ , respectively.

The predicted results of the four tests are presented in Fig. 11. And the difference profiles between the reference induced current,  $\bar{J}_{64to32}$  and the MoM  $\bar{J}_{32}$  are shown in Fig. 11(e). And the errors calculated with the second and third schemes are depicted in Fig. 11(f), and (g), respectively. It is observed from the results of Test#7 that excellent results can be got by both two input schemes compared to  $\bar{J}_{32}$  when the test profiles and the incident angle are all coincide with the training set.

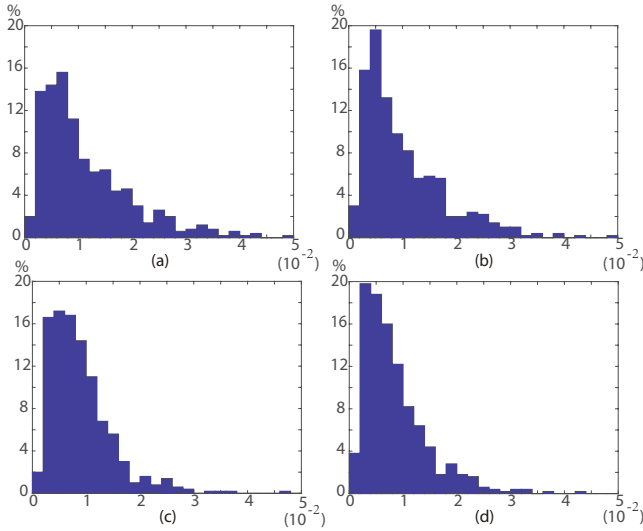


Fig. 12. The loss histograms over testing results for the multi-incidence case. (a) and (b) denote the histograms over MNIST test set with  $\bar{\chi} \cdot \bar{E}_p^{inc}$  and  $\bar{\chi} \oplus \bar{\chi} \cdot \bar{E}_p^{inc}$  as inputs of the network, respectively. (c) and (d) denote the histograms over “Cylinders” test set with  $\bar{\chi} \cdot \bar{E}_p^{inc}$  and  $\bar{\chi} \oplus \bar{\chi} \cdot \bar{E}_p^{inc}$  as inputs of the network, respectively.

However, in other test examples different from the training samples, although the performances of the predicted results are a little worse than that of Test #7, the results of FICLM are still better than the calculated one by MoM.

The detail information and predicted quantitative errors for the four tests are summarized in TABLE IV. From both the predicted induced current profiles in Fig. 11(f) and (g) and the quantitative errors in TABLE IV, it can be inferred that the proposed FICLM has better performance than the conventional MoM in terms of both the computational efficiency and accuracy when tackling the multi-incidence cases. Besides, an excellent generalization ability for the cases out of the training set (for both the profiles and the incidence angle) can be achieved by the proposed FICLM. From the statistical errors for the two test databases in TABLE IV and the histograms of tested results over the two test databases in Fig. 12, the performance by the third scheme is also better than the one by the second scheme in the multi-incidence case, which is consistent with the conclusion in the single-incidence.

Fig. 13(a)-(d) shows the calculated scattered fields (consisting of the real parts and imaginary parts) according to the predicted induced current for the Test #7-10, respectively. The calculated scattered fields at arbitrary angles by the proposed learning-based methods are quite coincide to the exact results calculated by the MoM with  $64 \times 64$  grids. Although there are very few deviations between the predicted scattered fields and the one calculated with MoM at some angles of the receivers, the results are quite satisfied. Therefore, for the multi-incidence case, the proposed learning-based forward solver with both second and third schemes all can well accurately predict the induced current and the third scheme exhibits better generalization capability to tackle with complicated problems.

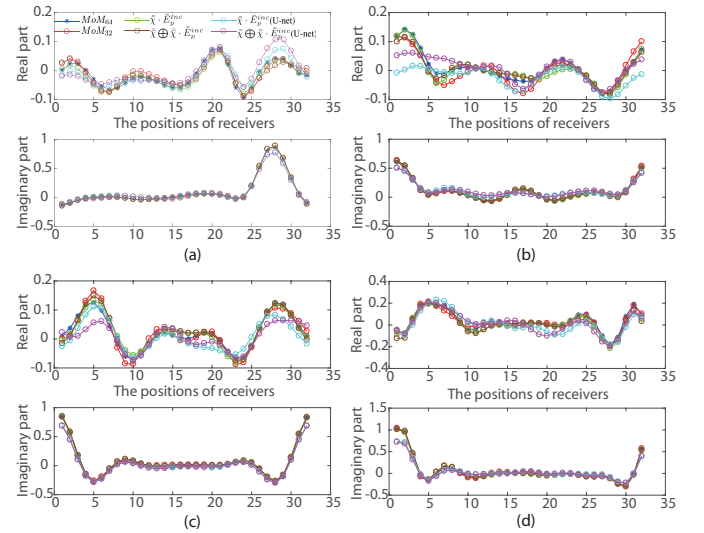


Fig. 13. The calculated scattered fields with the predicted induced currents in Fig. 11 for test# 7 to 10. (a) Test #7, (b) Test #8, (c) Test #9, (d) Test #10. The blue line “—” with “\*” is taken as a reference calculated by MoM using  $\bar{J}_{64}$ . The red line “—” with “o” denotes the scattered fields calculated by MoM with the induced current, i.e.,  $\bar{J}_{32 \times 32}$ . The green line “—” and the brown line “—” with “o” denote the results of scattered fields with the second and third schemes, respectively. The glaucous line “—” and the purple line “—” with “o” denote the scattered fields predicted with the second and third schemes by the U-net, respectively.

#### F. Test for multi-incidence case with U-net

Above we test the proposed FICLM with a pix2pix network model. In order to compare the performance of the proposed FICLM with some other neutral networks, the famous U-net, which is applied widely for image segmentation task, is also utilized to test the multi-incidence cases. In the training stage, the settings for both the samples and the neural network (e.g., the number of layers, the channels, batch sizes and so on) are the same as those in Section B.

The difference profiles between the predicted induced current by U-net and the reference one, i.e.,  $\bar{J}_{64to32}$  by MoM, are depicted in Fig. 11(h) and (i) for the second and third input schemes, respectively. As seen, compared to the difference profiles calculated by FICLM in Fig. 11(f) and (g), the errors of U-net are much larger. Consequently, the calculated scattered field has large deviation from the reference one by MoM<sub>64</sub> in Fig. 13, especially for the Test#8, Test#9 and Test#10. The quantitative results for the U-net are listed at the last two rows in TABLE IV. For both the Test#7-#10, the calculated errors are 4 to 8 times of the ones by the proposed FICLM. Further, from the statistical analysis in the last columns of TABLE IV, it is clearly drawn that, the calculated accuracy of the proposed FICLM is much better than the one of U-net.

## IV. DISCUSSIONS AND CONCLUSION

In this paper, we proposed a learning-based fast method to solve the EM scattering problems based on an end-to-end mapping of induced currents by a variant of generative adversarial network (GAN), namely the pix2pix model. The induced current instead of the scattered field is calculated

through a neural network with the proposed forward induced current learning method (FICLM). Then the scattered field can be obtained by a convolution of the Green's function with the induced current. Three schemes, i.e.,  $\bar{\chi}$ ,  $\bar{\chi} \cdot \bar{E}^{inc}$ ,  $\bar{\chi} \oplus \bar{\chi} \cdot \bar{E}^{inc}$ , have been proposed as the inputs of the network of FICLM. Physically, the  $\bar{\chi} \cdot \bar{E}^{inc}$  can be considered as an approximated induced current based on Born approximation, which means that an end-to-end mapping of neural networks from the input Born-type induced current to the true induced current is constructed.

Both the single-incidence and multi-incidence cases share the same structure of network. However, they were trained independently. The single-incidence case can be considered as a special one of the multi-incidence cases. In the single-incidence case, actually, when  $\bar{\chi}$  as input, in fact the proposed FICLM implicitly learning  $\bar{E}^{inc}$ . Therefore, when the incident intensity is fixed, the FICLM with all the three schemes can well approximate the mapping and predict the induced current accurately. However, if the incident intensity changes, considering the mappings of the first two schemes are physically not one-to-one, the third scheme shows better representation and generalization capabilities. In the multi-incidence cases, the second and third schemes incorporating the information of incident field have been utilized. The numerical simulations show that both schemes can well predict the induced currents even when the transmitting antenna is located at different angles and the scatterer profiles are out of the training range. From the statistical results of the two tested database, the third scheme of the proposed methods has better accuracy, versatility and stability compared with other two schemes for both single-incidence case and multi-incidence case. This is because the third scheme not only utilizes an end-to-end mapping of the induced current based on the Born approximation, but also provides additional information of contrast. This ensures to establish a one-to-one mapping to predict the induced current.

All the numerical simulations validate that the proposed FICLM exhibits better performance than the traditional MoM with the same grids in terms of computational efficiency and accuracy through use of reference data with a higher precision. With more accurate training sets obtained through off-line calculations by denser grids, the proposed FICLM can achieve better accuracy with the same computational source of the neural network. Compared with other neural networks, such as U-net, the proposed FICLM based on pix2pix model has better performance. Consequently, it is validated that the proposed learning-based FICLM method has several desired properties, such as good accuracy, two-step fast calculation, stability and generalization capacity, to solve the EM scattering problems. Though only 2-D cases are tested in our numerical experiments, the proposed approach can be easily customized to 3-D cases. In the future, we will also try to apply the proposed FICLM for solving 3-D electrically large EM scattering problems.

## REFERENCES

[1] N. K. Nikolova, *Introduction to Microwave Imaging*. Cambridge University, Press, 2017.

[2] M. S. Zhdanov, *Geophysical Inverse Theory and Regularization Problems*, Elsevier, US, 2002.

[3] A. Abubakar, P. M. V. D. Berg, and J. J. Mallorqui, "Imaging of biomedical data using a multiplicative regularized contrast source inversion method," *IEEE Trans. Microw. Theory Techn.*, vol. 50, no. 7, pp. 1761-1771, 2002.

[4] X. Wang, T. Qin, R. S. Witte, and H. Xin, "Computational feasibility study of contrast-enhanced thermoacoustic imaging for breast cancer detection using realistic numerical breast phantoms," *IEEE Trans. Microw. Theory Techn.*, vol. 63, no. 5, pp. 1489-1501, 2015.

[5] C. A. Balanis, *Antenna theory: analysis and design*. John Wiley & sons, 2016.

[6] X. Chen, *Computational Methods for Electromagnetic Inverse Scattering*. Hoboken, NJ, USA: Wiley, 2018.

[7] A. Sommerfeld, *Partial Differential Equations in Physics*. San Diego, CA, USA: Academic, 1949.

[8] A. F. Peterson, S. L. Ray, and R. Mittra, *Computational Methods for Electromagnetics*. Hoboken, NJ, USA: Wiley, 1998.

[9] W. C. Chew, *Waves and Fields in Inhomogeneous Media*. New York, NJ, USA: Van Nostrand, 1990.

[10] V. Thomee, "From finite differences to finite elements: A short history of numerical analysis of partial differential equations," *J. Comput. Appl. Math.*, vol. 128, no. 1, pp. 1-54, 2001.

[11] K. S. Yee and J. S. Chen, "The finite-difference time-domain (FDTD) and the finite-volume time-domain (FVTD) methods in solving Maxwell's equations," *IEEE Trans. Antennas Propag.*, vol. 45, no. 3, pp. 354-363, 1997.

[12] J. M. Jin, *The Finite Element Method in Electromagnetics*. New York, NY, USA: Wiley, 1993.

[13] P. K. Banerjee and R. Butterfield, *Boundary Element Methods in Engineering Science*. London, U.K.: McGraw-Hill, 1981.

[14] R. F. Harrington, *Field Computation by Moment Methods*. New York, NJ, USA: Wiley, 1993.

[15] W. C. Chew, J. M. Jin, E. Michielssen, and J. Song *Fast and Efficient Algorithms in Computational Electromagnetics*. Boston, MA: Artech House, 2001.

[16] F. Ling, C. F. Wang, and J. M. Jin, "An efficient algorithm for analyzing large-scale microstrip structures using adaptive integral method combined with discrete complex image method," *IEEE Trans. Microw. Theory Techn.*, vol. 48, pp. 832-837, 2000.

[17] X. C. Nie, N. Yuan, L. W. Li, Y. B. Gan, and T. S. Yeo, "A fast volume-surface integral equation solver for scattering from composite conducting-dielectric objects," *IEEE Trans. Antennas Propag.*, vol. 52, pp. 818-824, 2005.

[18] L. Greengard and V. Rokhlin, "A fast algorithm for particle simulations," *J. Comput. Phys.*, vol. 73, pp. 325-348, 1987.

[19] H. G. Wang, C. H. Chan, and L. Tsang, "A new multilevel Greens function interpolation method for large-scale low-frequency EM simulations," *IEEE Trans. Comput. Aided Des. Integr. Circuits Syst.*, vol. 24, no. 9, pp. 1427-1443, 2005.

[20] H. G. Wang and C. H. Chan, "The implementation of multilevel Greens function interpolation method for full-wave electromagnetic problems," *IEEE Trans. Antennas Propag.*, vol. 55, no. 5, pp. 1348-1358, 2007.

[21] I. Lagaris, A. Likas, and D. Fotiadis, "Artificial neural networks for solving ordinary and partial differential equations," *IEEE Trans. Neural Netw.*, vol. 9, no. 5, pp. 987-1000, 1998.

[22] P. Ramuhalli, L. Udpa, and S. Udpa, "Finite-element neural networks for solving differential equations," *IEEE Trans. Neural Netw.*, vol. 16, no. 6, pp. 1381-1392, 2005.

[23] J. An and Z. Ma, "Study on the solving method of electromagnetic field forward problem based on support vector machine," in *Proc. Conf. Mach. Learn. Cybern.*, pp. 1505-1509, 2010.

[24] A. Massa, G. Oliveri, M. Salucci, N. Anselmi, and P. Rocca, "Learning-by-examples techniques as applied to electromagnetics," *J. Electromagn. Waves Appl.*, vol. 32, no. 4, pp. 516-541, 2018.

[25] O. Ronneberger, P. Fischer, and T. Brox, "U-net: Convolutional networks for biomedical image segmentation," *Proc. 18th Int. Conf. Med. Image Comput. Comput. Assist. Intervent. (MICCAI)*, pp. 234-241, 2015.

[26] A. Krizhevsky, I. Sutskever, and G. E. Hinton, "ImageNet classification with deep convolutional neural networks," in *Proc. 25th Int. Conf. Neural Inf. Process. Syst.*, pp. 1097-1105, 2012.

[27] A. Massa, D. Marcantonio, X. Chen, M. Li, and M. Salucci, "DNNs as applied to electromagnetics, antennas, and propagation-a review," *IEEE Antennas Wireless Propag. Lett.*, vol. 18, no. 11, pp. 2225-2229, 2019.

[28] I. Giannakis, A. Giannopoulos, and C. Warren, "A machine learning-based fast-forward solver for ground penetrating radar with application

- to full-waveform inversion," *IEEE Trans. Geosci. Remote Sens.*, vol. 57, no. 7, pp. 4417-4426, 2019.
- [29] S. Chen, H. Wang, F. Xu, and Y. Q. Jin, "Target classification using the deep convolutional networks for SAR image," *IEEE Trans. Geosci. Remote Sens.*, vol. 54, no. 8, pp. 4806-4817, 2016.
- [30] Z. Wei and X. Chen, "Deep-learning schemes for full-wave nonlinear inverse scattering problems," *IEEE Trans. Geosci. Remote Sens.*, vol. 57, no. 4, pp. 1849-1860, 2018.
- [31] L. Li, L. Wang, F. Teixeira, C. Liu, A. Nehorai, and T. Cui, "DeepNIS: Deep neural network for nonlinear electromagnetic inverse scattering," *IEEE Trans. Antenna Propag.*, vol. 67, no. 3, pp. 1819-1825, 2018.
- [32] Z. Wei and X. Chen, "Physics-Inspired convolutional neural network for solving full-wave inverse scattering problems," *IEEE Trans. Antennas and Propag.*, vol. 67, no. 9, pp. 6138-6148, 2019.
- [33] R. Guo, X. Song, M. Li, F. Yang, S. Xu, and A. Abubakar, "Supervised descent learning technique for 2-D microwave imaging," *IEEE Trans. Antennas Propag.*, vol. 67, no. 5, pp. 3550-3554, 2019.
- [34] W. Tang, T. Shan, X. Dang, M. Li, F. Yang, S. Xu, and J. Wu, "Study on a Poisson's equation solver based on deep learning technique," *IEEE Elect. Des. Adv. Packag. Syst. Symp. (EDAPS)*, Hailing, China, pp. 1-3, 2017.
- [35] A. Khan, V. Ghorbanian, and D. Lowther, "Deep learning for magnetic field estimation," *IEEE Trans. Magn.*, vol. 55, no. 6, pp. 7202304, 2019.
- [36] P. Isola, J. Y. Zhu, T. Zhou, and A. A. Efros, "Image-to-image translation with conditional adversarial networks," *IEEE Int. Conf. on Computer Vision and Pattern Recognition*, 2017.
- [37] I. Goodfellow, J. Pouget-Abadie, M. Mirza, B. Xu, D. Warde-Farley, S. Ozair, A. Courville, and Y. Bengio, "Generative adversarial nets," *Adv. Neural Inf. Process. Syst.*, pp. 2672-2680, 2014.
- [38] T. Sarkar, E. Arvas, and S. Rao, "Application of FFT and the conjugate gradient method for the solution of electromagnetic radiation from electrically large and small conducting bodies," *IEEE Trans. Antennas and Propag.*, vol. 34, no. 5, pp. 635-640, 1986.
- [39] P. Zwamborn and P. M. van den Berg, "The three dimensional weak form of the conjugate gradient FFT method for solving scattering problems" *IEEE Trans. Microw. Theory Tech.*, vol. 40, no. 9, pp. 1757-1766, 1992.
- [40] A. Radford, L. Metz, and S. Chintala, "Unsupervised representation learning with deep convolutional generative adversarial networks," *arXiv preprint arXiv:1511.06434*, 2015.
- [41] M. Arjovsky, S. Chintala, and L. Bottou, "Wasserstein generative adversarial networks," *Proc. Int. Conf. Mach. Learn.*, pp. 214-223, 2017.
- [42] M. Mirza and S. Osindero, "Conditional Generative Adversarial Nets," *arXiv preprint arXiv:1411.1784*, 2014.
- [43] J. Y. Zhu, T. Park, P. Isola, and A. A. Efros, "Unpaired image-to-image translation using cycle-consistent adversarial networks," *IEEE Int. Conf. on Computer Vision*, pp. 2223-2232, 2017.
- [44] X. Mao, Q. Li, H. Xie, R. Lau, Z. Wang, and S. Smolley, "Least squares generative adversarial networks," *IEEE Int. Conf. on Computer Vision*, pp. 2794-2802, 2017.



as a Visiting Professor in 2018. Since September 2015, he has been with Hangzhou Dianzi University, Hangzhou, China, where he is now an associate Professor. His research interests include electromagnetic inverse problems, microwave measurement and novel antenna design.

**Kuiwen Xu** received the B.E. degree from Hangzhou Dianzi University, Hangzhou, China, in 2009, and the Ph.D. degree from Zhejiang University, Hangzhou, China, in 2014, all in electrical engineering. From 2012 to 2013, he was a Visiting Ph.D. Student with the National University of Singapore, Singapore. From 2014 to 2015, he was a Senior Researcher with Huawei Technologies Co., Ltd., Hangzhou, China. He was invited to the State Key Laboratory of Terahertz and Millimeter Waves at City University of Hong Kong, Hongkong, China,



**Zhenchao Ma** received the B.E. degree from Zhejiang University City College, Hangzhou, China, in 2017. He is currently pursuing the M.S. degree in Hangzhou Dianzi University. His current research interests include electromagnetic scattering problems and electromagnetic inverse scattering problems.



interests include intelligent perceptions for biomedical measurements, such as electromagnetic imaging, video-based physiological parameter measurement, and machine learning.

**Rencheng Song** received his B.S. degrees from Jilin University, Changchun, China, in 2005, and the Ph.D. degree from Zhejiang University, Hangzhou, China in 2010, both in computational mathematics. From 2010 to 2012, he was a Research Fellow with the National University of Singapore, Singapore. From 2013 to 2017, he was a Principal Scientist with Halliburton Far East Pte Ltd, Singapore. Since May 2017, he has been with the Department of Biomedical Engineering at Hefei University of Technology, Hefei, China, as an associate professor. His research



**Chao-Fu Wang** (M'98-SM'02) received the B.Sc. degree in mathematics from Henan Normal University, Xinxiang, China, in 1985, the M.Sc. degree in applied mathematics from Hunan University, Changsha, Hunan Province, China, in 1989, and the Ph.D. degree in electrical engineering from the University of Electronic Science and Technology of China, Chengdu, China, in 1995.

From 1987 to 1996, he was a Lecturer and then an Associate Professor with the Nanjing University of Science and Technology, Nanjing, China. From 1996 to 1999, he was a Postdoctoral Research Fellow with the Center for Computational Electromagnetics, University of Illinois at Urbana-Champaign. From 1999 to 2001, he was a Research Fellow with the Department of Electrical and Computer Engineering (ECE), National University of Singapore (NUS), Singapore. In 2001, he was transferred to the Temasek Laboratories (TL) at NUS, Singapore, as a Research Scientist, where he became a Senior Research Scientist in 2007 and a Principal Research Scientist in 2011. He has been leading TL Propagation and Scattering Group at NUS for many years to successfully conduct and accomplish research programs funded by Singapore Government. He co-authored *Characteristic Modes: Theory and Applications in Antenna Engineering* (Hoboken, NJ: Wiley, 2015). He has published more than 260 journal and conference papers, and filed six international WIPO/PCT patents. His research interests include fast and efficient algorithms for computational electromagnetics, theory of characteristic modes and its applications, fast design and analysis of antennas and antenna arrays, fast electromagnetic (EM) modeling and measurement of radio frequency integrated circuits, fast prediction of EM scattering from electrically large and complex objects, effective hybrid solution techniques for rapid EM design of real platform, efficient modeling of electromagnetic compatibility (EMC)/electromagnetic interference (EMI) for practical platform, multidisciplinary optimization and its applications, measurement of EM scattering and antenna, and real time simulation of EM imaging and processing. Dr. Wang successively served the IEEE Singapore Microwave Theory and Techniques (MTT)/Antennas and Propagation (AP) and EMC Chapters as a committee member, Secretary, Treasurer, and Vice-Chairman from 2003-2012. He served as a Chairman of the IEEE Singapore MTT/AP Chapter in 2013. He was a co-recipient of the 2009 Best Applied Computational Electromagnetics Society (ACES) Journal Paper Award. He has been actively involved in organizing several international conferences in Singapore. He has served as the Publication Chair of the 2005 IEEE International Symposium on Radio-Frequency Integration Technology (RFIT2005), RFIT2007, RFIT2012, and 2012 IEEE Asia-Pacific Conference on Antennas and Propagation (APCAP2012), the Organizing Committee Secretary of the 2005 IEEE International Workshop on Antenna Technology (IWAT2005) and 2006 International Symposium on Antennas and Propagation (ISAP2006), the Exhibition and Sponsorship Chair of the 2009 Asia Pacific Microwave Conference (APMC2009), the Exhibition Co-Chair of the 2018 Joint IEEE International Symposium on Electromagnetic Compatibility and Asia-Pacific Symposium on Electromagnetic Compatibility (2018 Joint IEEE EMC & APEMC Symposium), and Finance Chair of the IEEE APCAP2018. He is a General Chair of 2020 IEEE International Conference on Computational Electromagnetics (ICCEM 2020) and Special Session Chair of 2021 IEEE International Symposium on Antennas and Propagation and USNC-URSI Radio Science Meeting (IEEE AP-S/URSI 2021). As a regular reviewer of many international journals, he is currently an Associate Editor of the *IEEE Transactions on Microwave Theory and Techniques*, *IEEE Journal on Multiscale and Multiphysics Computational Techniques*, *International Journal of Numerical Modelling: Electronic Networks, Devices and Fields*, and *Electronics Letters*. As a Guest Editor of the *International Journal of Numerical Modelling: Electronic Networks, Devices and Fields*, he has successfully edited a special issue (volume 33, issue 2, March/April 2020) on advanced solution methods for modeling complex electromagnetic problems.



**Xudong Chen** (Fellow, IEEE) received the B.S. and M.S. degrees in electrical engineering from Zhejiang University, China, in 1999 and 2001, respectively, and the Ph.D. degree from the Massachusetts Institute of Technology, Cambridge, MA, USA, in 2005. Since 2005, he has been with the National University of Singapore, Singapore, where he is currently a Professor. He has published 150 journal papers on inverse scattering problems, material parameter retrieval, microscopy, and optical encryption. He has authored the book *Computational Methods for Electromagnetic Inverse Scattering* (Wiley-IEEE, 2018). His research interests include mainly electromagnetic wave theories and applications, with a focus on inverse problems and computational imaging. He is recently working on mm-wave imaging algorithms and solving inverse problems via machine learning. Dr. Chen was a recipient of the Young Scientist Award by the Union Radio Scientifique Internationale in 2010 and a recipient of the Ulrich L. Rohde Innovative Conference Paper Award at ICCEM 2019. He was an Associate Editor of the *IEEE Transactions on Microwave Theory and Techniques* during 2015-2019 and has been an Associate Editor of the *IEEE Journal of Electromagnetics, RF and Microwave in Medicine and Biology* since 2020. He has been members of organizing committees of more than 10 conferences, serving as General Chair, TPC Chair, Award Committee Chair, etc. He was the Chair of IEEE Singapore MTT/AP Joint Chapter in 2018. He is a Fellow of Electromagnetics Academy.